Superconductor Science and Technology

Transport properties of 2H-$NbSe_2$ synthesized by selenization of Nb thin films

OPEN ACCESS
IOP Publishing
Superconductor Science and Technology
Supercond. Sci. Technol. **37** (2024) 015020 (11pp)
https://doi.org/10.1088/1361-6668/ad1464

Transport properties of 2H-$NbSe_2$ synthesized by selenization of Nb thin films

A G Zaitsev, A Beck, D Fuchs, R Hott and R Schneider*

Institut für Quantenmaterialien und -technologien (IQMT), Karlsruher Institut für Technologie (KIT), Karlsruhe D-76021, Germany

E-mail: rudolf.schneider2@kit.edu

Received 24 July 2023, revised 24 November 2023
Accepted for publication 11 December 2023
Published 20 December 2023

Abstract

A novel method for the synthesis of 2H-$NbSe_2$ thin films by selenization of precursor Nb thin films is reported. The polycrystalline films grow predominantly in the hexagonal 2H-$NbSe_2$ phase with bulk lattice constants. Their remarkable microstructure consists of a three-dimensional network of flake-like grains substantially stacked vertically on the substrate. The electronic transport between 1.2 K and 300 K in zero and applied magnetic fields up to 14 T has been extensively studied. The study comprises resistivity, magnetoresistance, Hall coefficient, upper critical field, and critical current density. The results are discussed taking account of the coexisting charge-density-wave and superconducting phases.

Keywords: transition metal dichalcogenides, charge density wave, superconductivity

1. Introduction

The metallic layer material 2H-$NbSe_2$ belongs to the material class of transition metal dichalcogenides (TMDs) [1, 2]. It crystallizes in a highly anisotropic hexagonal (H) layered structure. The unit cell with bulk lattice constants $a = 0.344$ nm and $c = 1.254$ nm consists of two (2) single Se-Nb-Se monolayers rotated by 180° with respect to one another with a thickness of $c/2$ [3]. The Nb atom has as nearest neighbors 6 Se atoms arranged at the apices of a trigonal prism. This trigonal prism layer structure is stacked along the c-axis direction in a hexagonal close-packed AB sequence [4]. The intralayer bonding is covalent and strong, while the interlayer Se-Se bonding is weak due to van der Waals interaction between adjacent layers. For this reason bulk three-dimensional (3D) $NbSe_2$ crystals can be cleaved into two-dimensional (2D) flakes of a few layers and even monolayers [5]. Physical properties of the 2D material can be different from those of the 3D material.

The compound 2H-$NbSe_2$ is a conventional s-wave, phonon mediated, type II superconductor with the highest bulk superconducting transition temperature T_c of 7.2 K among the TMDs [6]. Two-band superconductivity is suggested by [7, 8] although an anisotropic s-wave single-band approximation cannot be excluded since electron-phonon coupling in one of the bands dominates [9, 10]. For bilayer and noncentrosymmetric monolayer the existence of a Bose-metal and Ising pairing in superconductivity has been reported, respectively [11, 12]. Superconductivity coexists with charge-density-wave (CDW) order in bulk and even single-layer 2H-$NbSe_2$ [13, 14] by opening the respective energy gaps on different parts of the Fermi surface. However, the magnitude of the gaps remains ambiguous [15–17].

The TMD 2H-$NbSe_2$ is a prototypical CDW system. The CDW phase is a macroscopic quantum state consisting of a periodic modulation of the electronic charge density accompanied by a periodic distortion of the crystal lattice. The triple incommensurate CDW order in 2H-$NbSe_2$ sets in at the temperature $T_{CDW} = 33$ K and is manifested, e.g. by an

* Author to whom any correspondence should be addressed.

anomaly in the resistivity and a drop with a sign reversal in the Hall coefficient. The transition has also strong optical signatures [18]. The resistivity is actually reduced in the CDW-ordered phase [19] that is insensitive to high magnetic fields as evidenced by x-ray scattering studies [20]. The origin of the bulk second-order phase transition remains controversial. According to [21] the origin of the CDW in 2H-$NbSe_2$ is well described by the momentum dependence of the electron-phonon-coupling matrix element, but not by Fermi surface nesting [22] or saddle-point singularities at the Fermi surface [23].

Various methods for the preparation of few-layer flakes and thin films of 2H-$NbSe_2$ are reported. By solvent-assisted or mechanical exfoliation flakes (also sheets or nanoplates) are separated from bulk single crystals [11, 12, 24–28]. Chemical exfoliation via lithium intercalation is also reported [29]. By means of molecular beam epitaxy (MBE) monolayers and single-crystalline films are deposited onto graphene, BN, SiO_x / Si and GaAs substrates [1, 14, 30, 31]. Few-layer nanoplates are produced by metal-organic (MO) and molten-salt assisted chemical vapor deposition [1, 32, 33]. Two-step vapor deposition methods for the selenization of transition metal precursor films are delineated in [34–37].

In this study a novel method for the synthesis of 2H-$NbSe_2$ thin films is reported. The process is composed of two steps: in the first step Nb thin films are deposited onto single-crystalline (001) oriented MgO substrates by conventional dc magnetron sputtering. In the second step these precursor films are transferred to an evacuated and heated reactor made of carbon where they are exposed to Se vapor for only a few minutes resulting in rapidly grown polycrystalline 2H-$NbSe_2$ thin films. The films are characterized with respect to their crystallographic structure and microstructure. The temperature-dependent resistivity and self-field critical current density are measured in zero magnetic field. Magnetoresistance, Hall coefficient, upper critical field and critical current density are determined for magnetic fields up to 14 T and temperatures down to 1.2 K.

The organization of this article mostly replicates that of a paper previously published by the authors [38].

2. Experimental

In the first step Nb precursor films with a typical thickness of 900 nm were deposited onto 5×5 mm^2 (001) oriented single-crystalline MgO substrates by high-power dc magnetron sputtering of a circular Nb target (99.9% purity, 75 mm diameter). The residual pressure in the vacuum chamber before deposition was 1×10^{-7} mbar. During deposition the substrate temperature was held at 850 °C, and the Ar operating pressure was 4×10^{-3} mbar. The Nb deposition rate amounted to 1 nm s^{-1}. The films were patterned *in situ* to 250 μm long and approximately 100 μm wide stripes by using metal masks fixed over the substrate. For the Hall measurements the pattern was like a cloverleaf [39]. The normal- and superconducting properties of the Nb stripes were excellent. The residual resistivity ratio RRR $= \rho(300\,\mathrm{K})/\rho(9.5\,\mathrm{K})$ amounted to a high value of

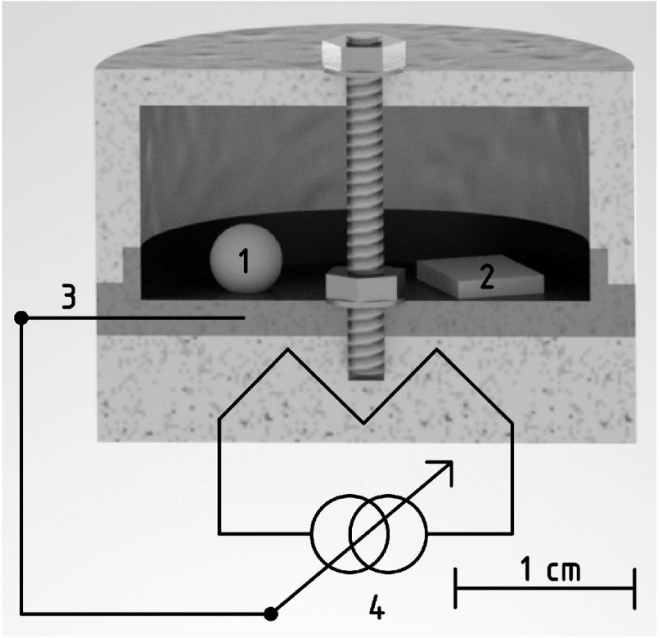

Figure 1. Cross section of the cylindrical two-piece carbon reactor (bottom + lid) for the vaporization of solid Se shots (1) and the selenization of Nb precursor films (2). The reactor is mounted on a stainless-steel resistively heated plate. (3) Sheathed NiCr-Ni thermocouple. (4) heater-current source with temperature controller.

22. $T_c = 9.4$ K with a transition width less than 0.1 K was even higher than the bulk value of 9.25 K [40] probably due to strain.

In the second step the vacuum chamber was vented with high-purity Ar. The freshly prepared patterned Nb precursor film was transferred to the reactor shown in figure 1 as fast as possible to minimize the exposure to nitrogen, oxygen, and moisture. The exposure to dry air was no longer than 5–10 min. The Se vapor source consisted of two amorphous Se shots with 99.999% purity (Alfa Aesar, 3–4 mm diameter, 60 mg weight per shot) placed next to the Nb film. The reactor mounted on a heater plate was made of carbon (alumina and BN were not suitable) that does not react with Se vapor at high temperature. The pressure in the reactor was reduced to 10^{-7} mbar in a second vacuum chamber. Thus, the $NbSe_2$ film was synthesized clean of nitrogen, oxygen, and water. As demonstrated in figure 2 the temperature of the reactor was increased to 800 °C within approximately three minutes and held for a few seconds. After switching off the heater the reactor with the fast-grown $NbSe_2$ film cooled down to 100 °C within 30 min. With 900 nm thick Nb precursor films the thickness of the resulting 2H-$NbSe_2$ films came to 3400 nm. This thickness increase by a factor of 3.8 corresponds to the ratio of the *c*-axis lattice constant of 2H-$NbSe_2$ ($c = 1.254$ nm) and the lattice constant of bcc-Nb ($a = 0.32986$ nm).

The film thickness was measured by a surface profilometer. X-ray (XRD) diffraction scans at room temperature revealed the crystallinity of the films. Scanning electron microscopy (SEM) enabled the study of the surface morphology. Direct current (dc) four-probe resistance and transport critical current measurements in the normal and superconducting state,

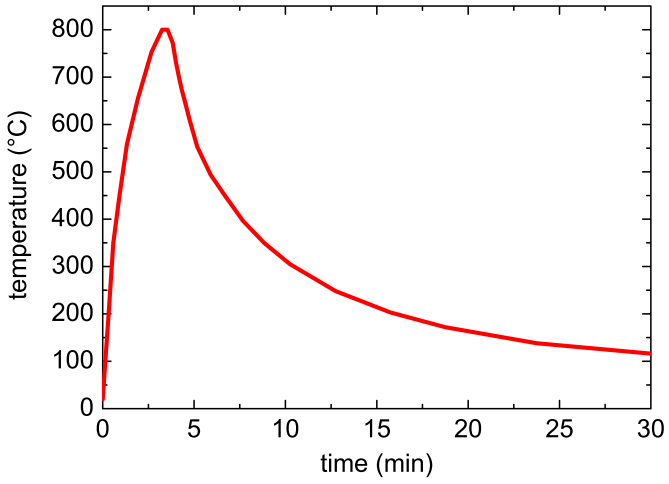

Figure 2. Temperature versus time profile for the selenization of Nb precursor films in the carbon reactor of figure 1.

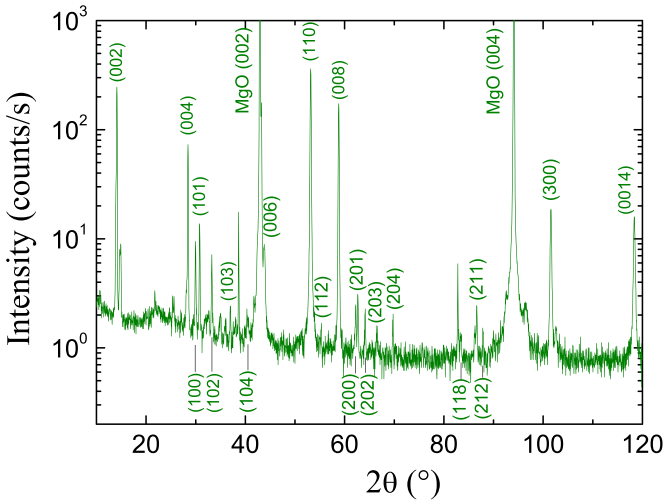

Figure 3. Θ–2Θ scan of a 3400 nm thick 2H-$NbSe_2$ film on (001) MgO substrate. Miller indices are allocated to the substrate and film reflections.

respectively, were carried out from room temperature to 1.2 K. Applied static magnetic fields normal and parallel to the film plane varied between zero and 14 T. The Hall measurements were performed by using the van der Pauw method [39, 41].

3. Results and discussion

3.1. Film crystallinity

A typical $\Theta-2\Theta$ XRD scan measured on a 3400 nm thick 2H-$NbSe_2$ film on a (001) oriented MgO substrate is shown in figure 3. The film grows in the hexagonal 2H-$NbSe_2$ phase ($P6_3/mmc$, space group No. 194) with lattice constants $a =$ 0.344 nm and $c = 1.254$ nm in accordance with the values for bulk powder samples [42]. The reflections with the strongest intensities can be indexed by (00ℓ) ($\ell = 2, 4, 6, 8, 14$) and reveal a rudimentary epitaxial c-axis growth of $NbSe_2$ [001] || [001] MgO with a broad mosaic spread of 1.3° and an in-plane oriantational relationship $NbSe_2$ [100] || [100] MgO inferred from the respective ω— and Φ— scans. There are, in addition, a textured growth of (110) oriented grains with a broad mosaic spread of $\omega = 5.5°$ and polycrystalline grains. A tiny admixture of foreign phases, among them presumably Se and Nb_2Se_3, can also be found.

3.2. Film surface

The SEM micrograph in figure 4 displays flake-like flat grains that are presumably single-crystalline and consist of parallel Se-Nb-Se layers. The size of the flakes and their thickness are estimated at a few microns and 400–1000 monolayers. A substantial amount of the flakes are stacked vertically on the substrate with random azimuthal orientation. They form a 3D network with the remaining randomly tilted or horizontally stacked flakes, which the observed epitaxy can be ascribed to.

A similar microstructure is also reported in [36] for bulk-like polycrystalline 2H-$NbSe_2$ films prepared by selenization

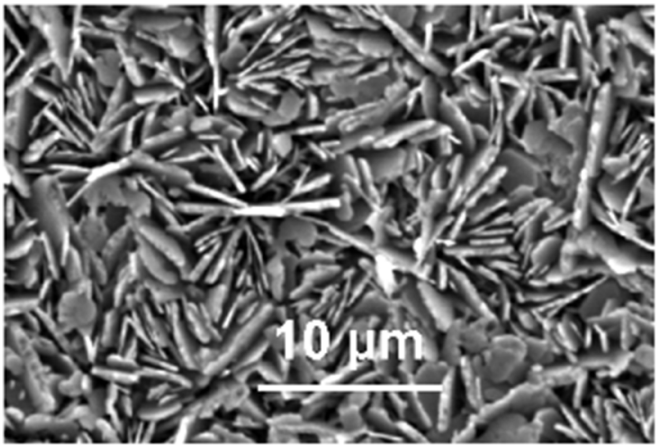

Figure 4. SEM micrograph of the surface of the 3400 nm thick 2H-$NbSe_2$ film on (001) MgO substrate showing a combination of vertically and horizontally (parallel to the substrate surface) aligned and randomly tilted flakes.

of Nb precursor films on SiO_2 / Si substrates in a two-step vapor-phase reaction under ambient pressure by using a two-zone furnace.

3.3. Electronic transport in zero magnetic field

3.3.1. Resistivity. The temperature-dependent dc resistivity ρ from 7 K to room temperature of a 100 μm wide 2H-$NbSe_2$ stripe is shown in figure 5(a). The profile looks similar to those reported in [43, 44] for single crystals. The resistivity ρ_{RT} at room temperature (RT $\approx$ 300 K) of 478 $\mu\Omega$ cm and the residual resistivity ρ_{res} at 7.5 K of 35 $\mu\Omega$ cm in the polycrystalline film are significantly higher than the corresponding values for the single crystals in [43, 44]. The residual resistivity ratio RRR $= \rho_{RT}/\rho_{res}$ of 13.6 is substantially lower than RRR of the single crystals, nevertheless, relatively high for a thin film. Between 7.5 K and 18 K, above the transition temperature

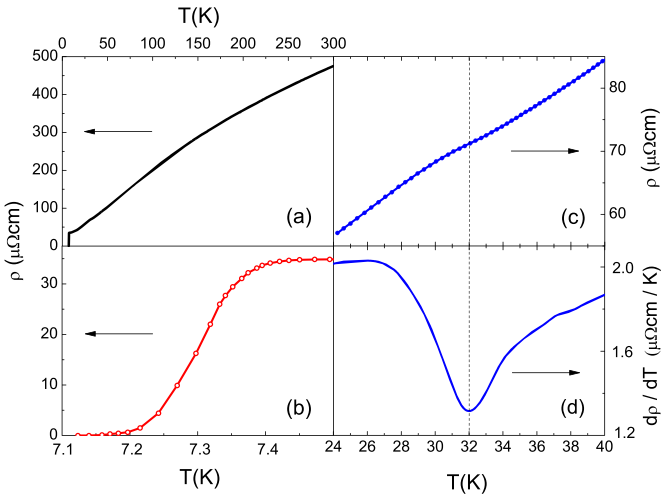

Figure 5. (a) dc resistivity ρ versus the temperature T. (b) Magnification of (a) in the temperature range 7.1 K–7.5 K demonstrating the residual resistivity and the resistive transition to superconductivity. (c) Magnification of (a) in the temperature range 24 K–40 K. The hump at 32 K indicates the onset of the CDW phase. (d) First derivative $\mathrm{d}\rho/\mathrm{d}T$ of (c) to elucidate the onset of CDW order by the minimum at 32 K.

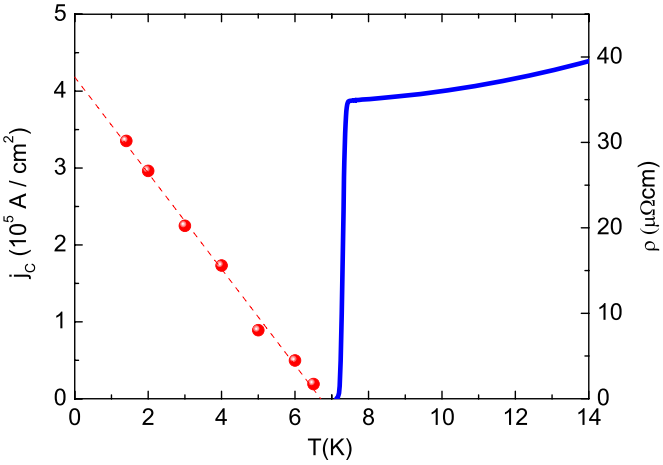

Figure 6. Left scale: critical current density j_c versus temperature between 1.3 K and 7 K. Right scale: resistivity ρ versus temperature between 7 K and 14 K. The dashed line is a fit $j_c(t) \propto (1-t)$ with $t = T/T_c$.

T_c to superconductivity and below the transition temperature T_{CDW} to the CDW phase, the temperature dependent part of the resistivity $\rho_T = \rho - \rho_{res}$ displays a cubic T^3 - dependence in accordance with [44, 45]. In a two-band model by Wilson [46] a cubic temperature dependence is expected for electron-phonon interband scattering between bands of high and low mobility (see also 3.4.2.) In the low-temperature range below 18 K the resistivity also manifests adherence to Matthiessen's rule $\rho = A + BT^n$ that expresses the temperature-independent contribution to ρ due to scattering by lattice imperfections and the separate contribution due to a temperature-dependent process such as electron-phonon scattering. The value of the exponent n depends on the specific scattering mechanism. Above T_{CDW} up to ≈110 K ρ_T reveals a linear behavior $CT + D$ with $D < 0$ suggestive of usual electron-phonon scattering. In a normal metal, however, $D = 0$ and ρ_T is generally proportional to the temperature above the Debye temperature Θ_D. For 2H-$NbSe_2$, $\Theta_D \approx 160$ K [44] is much above the temperature range of the observed linearity, questioning that 2H-$NbSe_2$ is a normal metal. Above 110 K ρ_T deviates from linearity with a negative curvature up to 300 K.

The resistive transition to superconductivity together with the residual resistivity is demonstrated in figure 5(b). The 90% ρ_{res} onset temperature, the 50% ρ_{res} midpoint temperature and the 10% ρ_{res} downset temperature amount to 7.37 K, 7.30 K, and 7.23 K, respectively, resulting in a 90% to 10% transition width $\Delta T_c = 0.14$ K. Such a small value hints to a homogeneous sample.

The anomaly at $T_{CDW} = 32$ K in figure 5(c) is the signature of the onset of CDW ordering. At this temperature the first derivative $\mathrm{d}\rho/\mathrm{d}T$ has a minimum as shown in figure 5(d). With the onset of the CDW phase $\rho(T)$ changes the slope and drops more rapidly below T_{CDW}. This is explained in terms of van Hove singularities driving the CDW phase and acting as scattering centers above T_{CDW} which are removed from the CDW phase [19]. In [44] the more rapid drop is explained by phase ordering of the CDW, i.e. the absence of impurity-like phase disorder scattering due to local CDW fluctuations. The observation of the anomaly in the polycrystalline film with a relatively low RRR of merely 13.6 might be astonishing, since in [47, 48] the authors argue that single crystals with RRR around 30 or higher are needed to observe a CDW anomaly in the temperature dependent resistivity. The weakness or vanishing of the anomaly is ascribed to a distortion of the CDW phase order in samples with lower RRR [48]. In our opinion figures 5(c) and (d) confirm a high CDW phase order with large CDW domains and few domain boundaries that enable the observation of the anomaly in the resistivity despite the low RRR.

3.3.2. Self-field critical current density. The self-field transport critical current density $j_c(T) = I_c(T)/A$ of the superconducting stripe was measured in dependence on the temperature. I_c is the critical current determined from voltage-current characteristics, and $A = 4.1 \times 10^{-6}$ cm^2 is the cross-sectional area of the stripe measured by using a surface profilometer. The I_c criterion is the well-recognized field-strength $E_c = 1\mu$V cm^{-1}.

$j_c(T)$ is shown in figure 6 from 1.3 K to 7 K together with the resistivity from 7 K to 14 K (cf Figure 5(b)). j_c is in the order of magnitude 10^5 A cm^{-2} which is a factor of 10 larger than 10^4 A cm^{-2} reported for 2H-$NbSe_2$ single crystals of stoichiometric composition in zero magnetic field [49]. This comparison with single crystals suggests that the grain boundaries in the polycrystalline film (the contacts between the flakes in figure 4) function as strong links enabling a high j_c.

For a quantitative description of $j_c(T)$ a proximity-effect model based on de Gennes' theory is employed [50, 51]. The model predicts a power-law dependence of $j_c(t) = j_c(0)(1-t)^{\beta}$ with the reduced temperature $t = T/T_c$. The

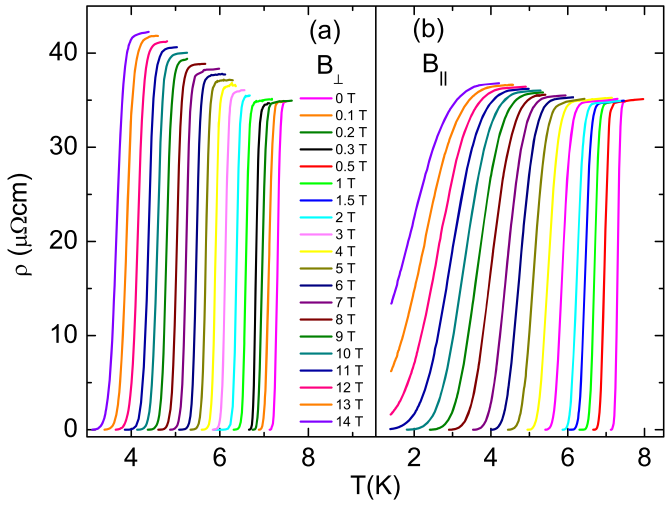

Figure 7. Resistivity $\rho\,(T,\,B)$ in a static magnetic field perpendicular ($B_\perp$) (a) and parallel ($B_\parallel$) (b) to the film plane.

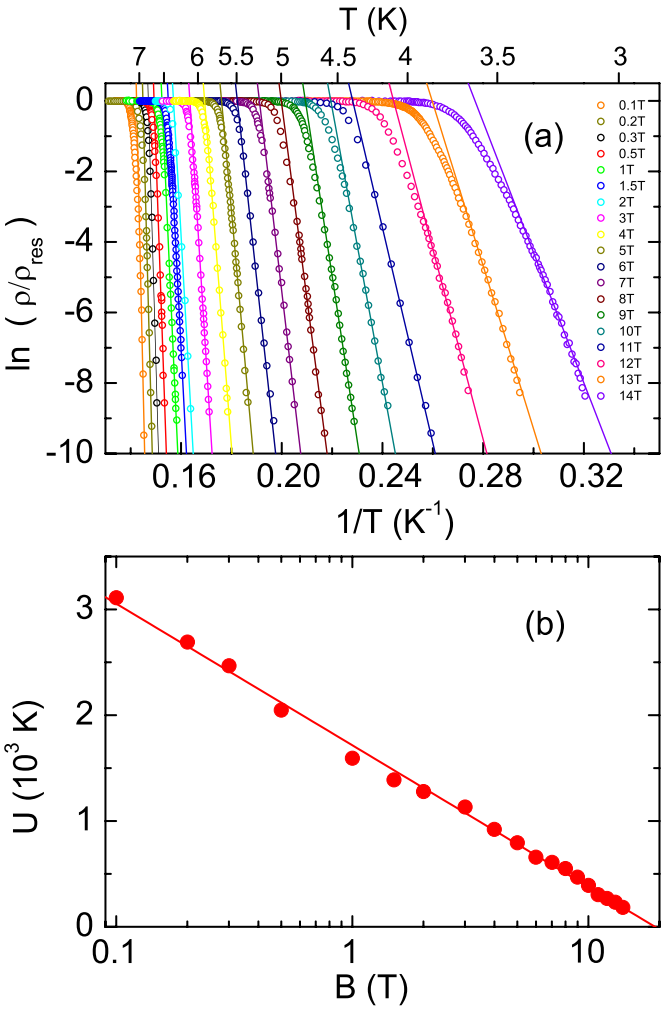

Figure 8. (a) Arrhenius plot of the resistivity data in figure 7(a) normalized to the residual resistivity $\rho_{\rm res}\,(B)$ with the transverse magnetic field $B_\perp$ from 0.1 T to 14 T as a parameter (open circles). The data points are fitted by the solid lines according to the TAFF theory. (b) Thermal activation energy $U(B)$ (full circles) and logarithmic fit (solid line) in a semi-log plot.

exponent β depends on the type of the junction, e.g. $\beta = 1$ for superconductor-insulator-superconductor S-I-S tunnel junctions. The $j_{\rm c}\,(T)$ data in figure 6 can be well fitted by $j_{\rm c}\,(t) \propto (1-t)$. The exponent $\beta = 1$ implies that the thin boundaries acting as tunnel barriers in the 3D network of 2H-$NbSe_2$ flakes in figure 4 consist of insulating potentially Se-deficient material.

The $j_{\rm c}\,(T)$ measurement and particularly its analysis build upon our previous work on FeSe thin films [38]. In that work a different exponent $\beta = 2$ was found suggesting normal conducting grain boundaries.

Concerning the larger $j_{\rm c}$ values in comparison to a single crystal an explanation alternative to the proximity-effect model is provided by enhanced pinning of vortices in the self-field at corrugations of the inherently rough film surface [52, 53]. This approach is supported by the results discussed in 3.4.4. Where surface pinning turns out an important pinning mechanism in the mixed state.

3.4. In-field electronic transport

3.4.1. Magnetoresistance. A static magnetic field was applied perpendicular ($B_\perp$) and parallel ($B_\parallel$) to the film plane. In the figures 7(a) and (b) the resistivity $\rho\,(T,\,B)$ for $B_\perp$ and $B_\parallel$ is shown for temperatures T from 1.2 K to 8 K with the magnetic induction B as a parameter from 0 to 14 T. With increasing B $T_{\rm c}$ is stronger reduced for $B_\parallel$ than for $B_\perp$. There is a parallel shift of the transition curves at low fields. A significant broadening of the transition occurs beyond 7 T for $B_\perp$ and 1 T for $B_\parallel$. Regarding the low-field shift the 2H-$NbSe_2$ film resembles conventional low-$T_{\rm c}$ superconductors [54]. In the normal state, just above $T_{\rm c}$, the residual resistivity increases with decreasing T and increasing B. The increase is visibly stronger for $B_\perp$.

The resistive transition to superconductivity, i.e. the field and temperature dependent drop of the resistivity in figure 7, is analyzed in terms of thermally activated flux flow (TAFF) [55, 56]. The TAFF model assumes pinning of the flux line lattice and creep-type motion of vortices in the mixed state of a type II superconductor due to thermal fluctuations if the energy barrier $U(B)$ for the vortex motion is finite and much higher than the temperature. For a given field-dependent barrier height the resistivity decreases exponentially with decreasing temperature: $\rho\,(T,\,B) = \rho_{\rm res}(B)\,\exp\,(-U\,(B)/\,T)$. This behavior is demonstrated by the Arrhenius plot in figure 8(a) where $\ln\,(\rho/\rho_{\rm res})$ versus $1/T$ (with the $\rho\,(T,\,B)$ values from figure 7(a)) is plotted with $B_\perp$ as a parameter from 0.1 to 14 T. The solid lines are fits using the above equation of the TAFF theory. The field dependent thermal activation energy $U(B)$ is shown in figure 8(b). The data points (full circles) can be fitted by the logarithmic dependence $U\,(B) = U_0\,\ln\,(B_0/B)$ with $U_0 = 581$ K and the melting field of the vortex lattice $B_0 = 19.2$ T (solid line). At $B = B_0$ the pinning potential is zero, and the Lorentz force produced by a current leads to a flux flow state in the absence of pinning with finite resistivity $\rho = \rho_{\rm res} \times (B/\,B_{\rm c2})$ [56, 57]. The dimensionality of the vortex

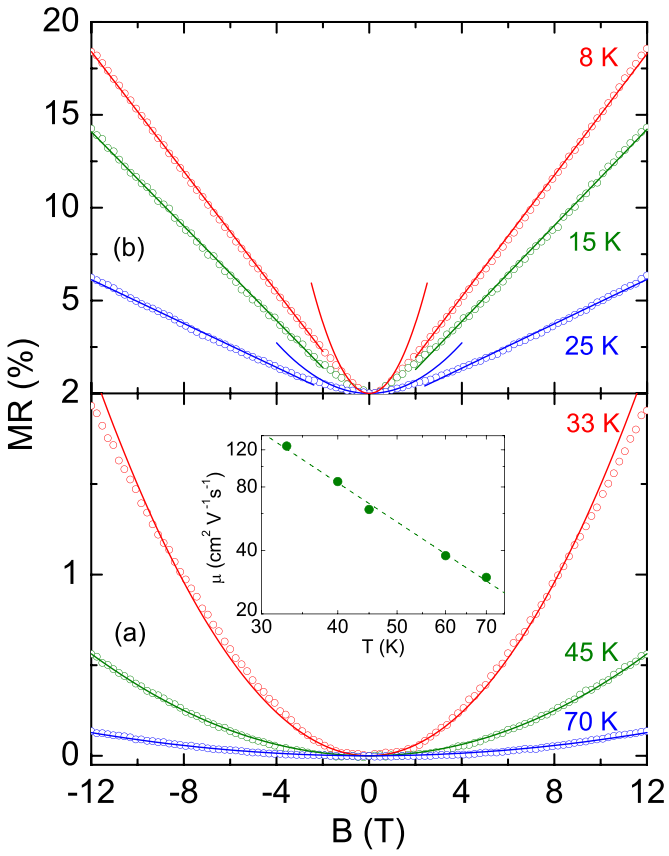

Figure 9. Magnetoresistance $MR(B,T)$ in the low-field regime $\mu B \ll 1$ at temperatures above (a) and below (b) T_{CDW}. The solid lines are quadratic and linear fits to the data points (open circles). The inset in (a) shows the temperature dependence of the effective mobility $\mu(T)$ that is used as a fitting parameter for the parabola in (a). The dashed line is a power-law fit.

matter leads to a specific field dependence of U. The logarithmic dependence, that was also found for mono- and bilayer 2H-$NbSe_2$ [11, 58] with clearly lower activation energies compared to our bulk-like films, suggests a quasi 2D 'pancake' vortex matter as it is expected for layered superconductors in a transverse magnetic field [59]. The results for the field parallel to the film plane ($B_{\parallel}$) are very similar to those in figure 8. $U_0 = 730$ K is higher and $B_0 = 11.4$ T lower. The small difference suggests that the pinning forces weakly depend on the field orientation.

The transverse ($B_{\perp}$) magnetoresistance $MR(B,T) = (\rho(B,T) - \rho(0,T))/\rho(0,T)$ in the normal state from 70 K to 8 K is shown in figure 9. *MR* is small, positive, symmetric to the vertical axis and increasing with increasing field and decreasing temperature. At $T > 33$ K (figure 9(a)), above the CDW transition, *MR* amounts to less than 2%. The curves can be fitted by a Lorentzian function $MR(B,T) = (\mu(T)B)^2/[1+(\mu(T)B)^2]$ that is reduced to $MR(B,T) \approx (\mu(T)B)^2$ for $\mu B \ll 1$ (solid lines in figure 9(a)). μ is an effective *MR* mobility of electrons and holes. In a semiclassical approach for a two-charge-carrier system such as 2H-$NbSe_2$ (cf 3.4.2.) μ depends on the electron and hole carrier densities n_e, n_h and mobilities μ_e, μ_h:

$$\mu = (n_e\,|\mu_e|\,n_h\,\mu_h)^{0.5}(n_e\,|\mu_e| + n_h\,\mu_h)^{-1}\,(|\mu_e| + \mu_h)\,.$$

The quadratic growth for $\mu B \ll 1$ is predicted by the conventional theory of *MR* in a metal with nonequal densities of electrons and holes [60]. Since $\mu B \gg 1$ is not met in this study, saturation or further quadratic growth in the case of compensation, i.e. equal densities of electrons and holes, is not observed. The temperature dependence of the mobility $\mu(T)$ is displayed in the inset of figure 9(a). μ increases with decreasing T up to a small value of 125 $cm^2\ V^{-1}\ s^{-1}$ at 33 K. A power-law dependence $\mu(T) \propto T^{-\delta}$ with $\delta \approx 1.9 \pm 0.1$ is an appropriate fit to the data points. The exponent δ close to 2 points to Fermi-liquid behavior.

The value of *MR* increases significantly with decreasing T below T_{CDW} and reaches a value of 18% at 8 K and 12 T (figure 9(b)). The shape of the curves remarkably changes from weak-field quadratic below $B \approx 2$ T to high-field linear for $B \gtrsim 2$ T (solid lines in figure 9(b)), possibly triggered by the CDW order. The anomalous linear dependence on magnetic field strength was already observed for 2H-$NbSe_2$ single crystals [61, 62]. The slope of the linear *MR* increases from 25 K to 8 K by almost a factor of 3. There are many reports on linear *MR* in various materials such as potassium [63], the heavily disordered silver chalcogenides $Ag_{2-\delta}Se$ and $Ag_{2-\delta}Te$ [64], graphene [65], 2D layered $SrMnBi_2$ [66], the topological insulator $Bi_{1.5}Sb_{0.5}Te_{1.7}Se_{1.3}$ [67], and the iron-based superconductors Ba(Sr)Fe_2As_2 [68] and $FeSe_{0.4}Te_{0.6}$ [69].

Linear or quantum *MR* can be interpreted in terms of a quantum limit [70] where all the charge carriers occupy only the lowest Landau level. It is associated with the existence of high-mobility Dirac fermions that dominate the electronic transport. A certain possibility of linear *MR*, however, exists in a polycrystalline metal with an open Fermi surface [60]. Regarding the 2H-$NbSe_2$ films in this work further studies are needed to investigate the scenario of Dirac fermions, in particular the study of the temperature dependence of the crossover field from quadratic to linear behavior of *MR*. Since linear *MR* in 2H-$NbSe_2$ occurs below T_{CDW} it is suggestive that the charge density wave is responsible for the effect. In [61–63] it is pointed out that the existence of CDW energy gaps provides a scattering mechanism, and the linear *MR* has been tentatively attributed to magnetic breakdown of the gaps.

3.4.2. Low-field Hall coefficient. The magnetic field dependence of the Hall resistivity ρ_{xy} at 200 K, 33 K, 20 K, and 7.5 K is shown in figures 10(a)–(d), respectively. The field range, where ρ_{xy} depends linearly on B, is shrinking with decreasing temperature. Whereas the linear range reaches from −12 T to 12 T at 200 K, it merely reaches from −0.75 T to 0.75 T at 7.5 K. For this low-field region, we define the low-field Hall coefficient $R_H = \rho_{xy}/B$ for all the temperatures. The temperature dependence of R_H is displayed in figure 11. R_H is positive which means that the majority carrier type is hole-like. Above 200 K R_H is apparently constant. Between 200 K and the onset of the CDW transition at 32 K R_H increases and sharply drops in the CDW phase. A change of the sign of R_H is not observed in our films.

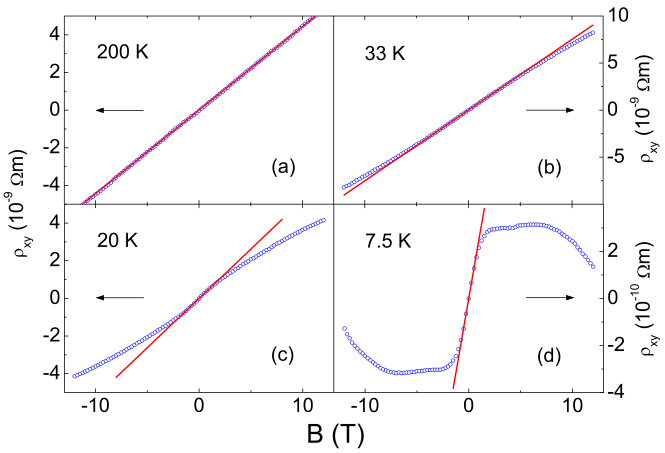

Figure 10. Measured magnetic field dependence of the Hall resistivity ρ_{xy} at 200 K (a), 33 K (b), 20 K (c), and 7.5 K (d) (open circles). The solid lines indicate the temperature-dependent field range where $\rho_{xy}(B,T) = R_{\rm H}(T) \times B$.

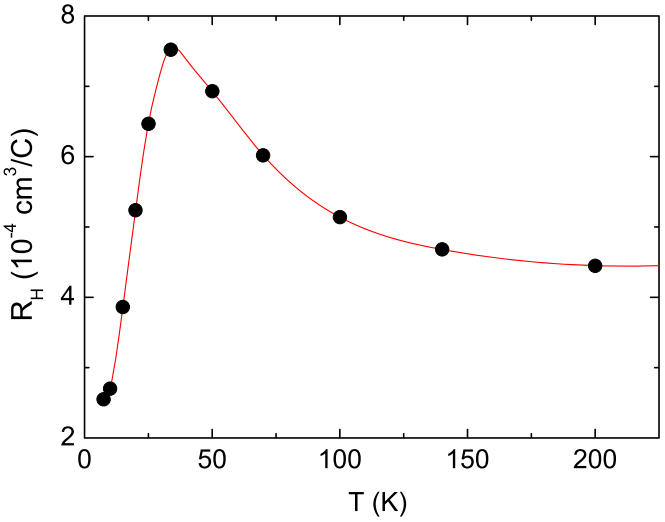

Figure 11. Low-field Hall coefficient $R_{\rm H}$ versus temperature. The solid line through the data points is a guide to the eye.

$R_{\rm H}$ of the films can be compared to $R_{\rm H}$ of 2H-$NbSe_2$ single crystals and bilayers. In pure high RRR single crystals $R_{\rm H}$ is positive and nearly constant down to 50 K to 40 K where a rapid drop starts accompanied by a sign reversal at around 25 K to 30 K [3, 71–73]. On the other hand no sign reversal and increase with and without a drop is observed in impure low RRR single crystals and bilayer 2H-$NbSe_2$ [72–74].

In order to estimate the hole and electron carrier densities $n_{\rm h}$, $n_{\rm e}$ and their mobilities $\mu_{\rm h}$, $\mu_{\rm e}$ the magnetoresistance *MR* of the same sample was also measured at 200 K where $R_{\rm H}$ starts to be constant with increasing temperature (see figure 11). In a semiclassical approach $R_{\rm H}$ and *MR* of a two-charge-carrier system in the low field region are given by [75, 76]:

$$R_{\rm H} = {\rm e}^{-1}\left(n_{\rm h}\,\mu_{\rm h}^2 - n_{\rm e}\,\mu_{\rm e}^2\right)/\left(n_{\rm h}\,\mu_{\rm h} + n_{\rm e}\,|\mu_{\rm e}|\right)^2 \text{ and}$$

$$MR = (\mu B)^2 = n_{\rm h}\,\mu_{\rm h}\,n_{\rm e}\,|\mu_{\rm e}|\left(n_{\rm h}\,\mu_{\rm h} + n_{\rm e}\,|\mu_{\rm e}|\right)^{-2}(\mu_{\rm h} + |\mu_{\rm e}|)^2\,B^2.$$

A simultaneous fit of the experimental ρ_{xy} (200 K) (see figure 10(a)) and *MR* (200 K) (not shown) provides $n_{\rm h} = 9 \times 10^{21}$ cm^{-3}, $n_{\rm e} = 4 \times 10^{19}$ cm^{-3}, $\mu_{\rm h} = 13$ cm^2 V^{-1} s^{-1}, $\mu_{\rm e} = 100$ cm^2 V^{-1} s^{-1}, $n_{\rm h}/n_{\rm e} = 225$, $\mu_{\rm e}/\mu_{\rm h} = 7.7$. Using the formulae of Wilson's two-band model [77] and assuming temperature-independent carrier densities Huntley and Frindt [72] determined for their single crystals $n_{\rm h} = (8.8 \pm 0.8) \times 10^{21}$ cm^{-3} and $n_{\rm e} = (4.2 \pm 0.6) \times 10^{19}$ cm^{-3} with $n_{\rm h}/n_{\rm e} = 210$ corresponding to about 1 hole per 2 Nb atoms and 3 electrons per 1000 Nb atoms. The carrier mobilities were assumed to be temperature dependent due to scattering with phonons at high temperature and impurities at low temperature, e.g. $\mu_{\rm h} = 10$ cm^2 V^{-1} s^{-1}, $\mu_{\rm e} = 80$ cm^2 V^{-1} s^{-1} with $\mu_{\rm e}/\mu_{\rm h} = 8$ at 200 K and $\mu_{\rm h} = 100$ cm^2 V^{-1} s^{-1}, $\mu_{\rm e} = 2000$ cm^2 V^{-1} s^{-1} at 20 K. The reasonable agreement with our values above confirms the scenario of holes of high density and low mobility and electrons of much lower density and much higher mobility also in the thin films. The existence of electron and hole bands is compatible with the T^3 dependence of the resistivity at low temperature (see 3.3.1).

3.4.3. Upper critical field. The temperature dependent upper critical field $B_{\rm c2}(T)$ is determined from the $\rho\ (T,\ B)$ curves in figure 7 as the field at which ρ is 90% of the residual resistivity. The result is shown in figure 12 for $B_\perp$ and $B_\parallel$ from 0 to $T_{\rm c} = 7.3$ K and 0–14 T. $B_\perp$ and $B_\parallel$ mean the applied magnetic field perpendicular and parallel to the substrate surface or film plane, respectively. In our polycrystalline 2H-$NbSe_2$ thin films these field orientations are not necessarily perpendicular and parallel to the Se-Nb-Se layers, in contrast to single crystals and *c*-axis oriented epitaxial thin films. Just below $T_{\rm c}$ there is a fairly good agreement with the single crystal data by Leupold *et al* [78] (dashed lines in figure 12). However, whereas $B_{\rm c2}(T)$ of the single crystal increases linearly with $B_{\rm c2}^{\parallel} > B_{\rm c2}^{\perp}$ (here, $\parallel$ and $\perp$ mean parallel and perpendicular to the Se-Nb-Se layers) when T decreases, our $B_{\rm c2}(T)$ thin-film curves have a crossing point at 6.4 K and 2 T where $B_{\rm c2}^{\perp}$ becomes larger than $B_{\rm c2}^{\parallel}$ (see inset in figure 12). Moreover, the curves show a positive curvature for both field orientations down to the inflection points at 5.3 K and 7 T for $B_\perp$ and at 5.2 K and 6 T for $B_\parallel$. The temperatures of 5.3 K and 5.2 K are close to the temperature 5.6 K reported in [79]. At the inflection points the $B_{\rm c2}(T)$ curves change from positive curvature to a linear behavior with decreasing T. The extrapolation of the linear fit to zero temperature results in $B_{\rm c2}^{\parallel}(0) = 23$ T and $B_{\rm c2}^{\perp}(0) = 32$ T. These values are larger than those reported for the single crystal (16 T for $B_\parallel$ and 6 T for $B_\perp$).

Although not observed in the single-crystal data of [78], positive curvature and, in addition, extended linearity down to low temperature seem to be typical for 2H-$NbSe_2$, as reported in [80–82]. Positive curvature is also observed in other layered superconductors, namely superconducting multilayers Nb/$Nb_{0.6}Ti_{0.4}$ [83], electron-doped high-temperature superconductors $L_{2-x}Ce_xCuO_{4-y}$ (L = Sr, Sm, Nd) [84], $K_xBa_{1-x}BiO_3$ high-temperature superconductor single crystals [85] and

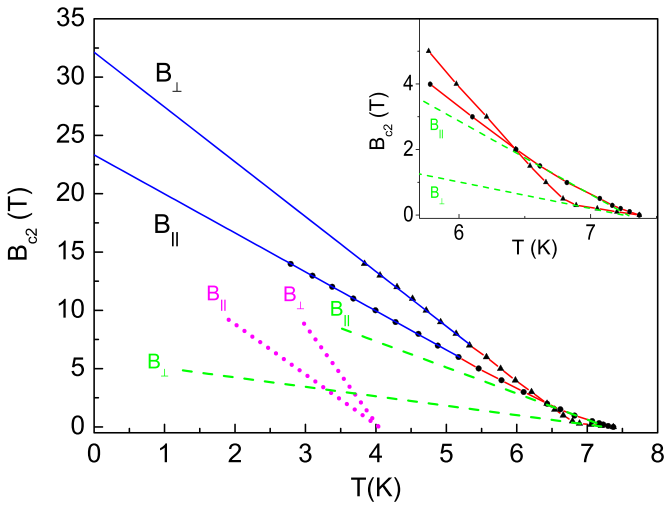

Figure 12. Anisotropic upper critical field $B_{c2}(T)$ versus T for $B_\perp$ and $B_\parallel$ perpendicular (up triangles) and parallel (circles) to the film plane, respectively. The blue solid lines left from the inflection points (5.3 K | 7 T) for $B_\perp$ and (5.2 K | 6 T) for $B_\parallel$ are linear fits extrapolated to zero temperature. The red lines right from the inflection points are guides to the eye. The inset demonstrates the crossing point (6.4 K | 2 T) where $B_{c2}^{\perp}$ becomes larger than $B_{c2}^{\parallel}$ with decreasing T. The dashed lines display data measured on a single crystal [78] where $B_{c2}^{\parallel} > B_{c2}^{\perp}$ over the entire temperature range. The dotted lines represent polycrystalline thin-film data [36] with $B_{c2}^{\perp} > B_{c2}^{\parallel}$ due to a dedicated film morphology. The inset also demonstrates the agreement of our thin-film data with the single-crystal data just below $T_c = 7.3$ K.

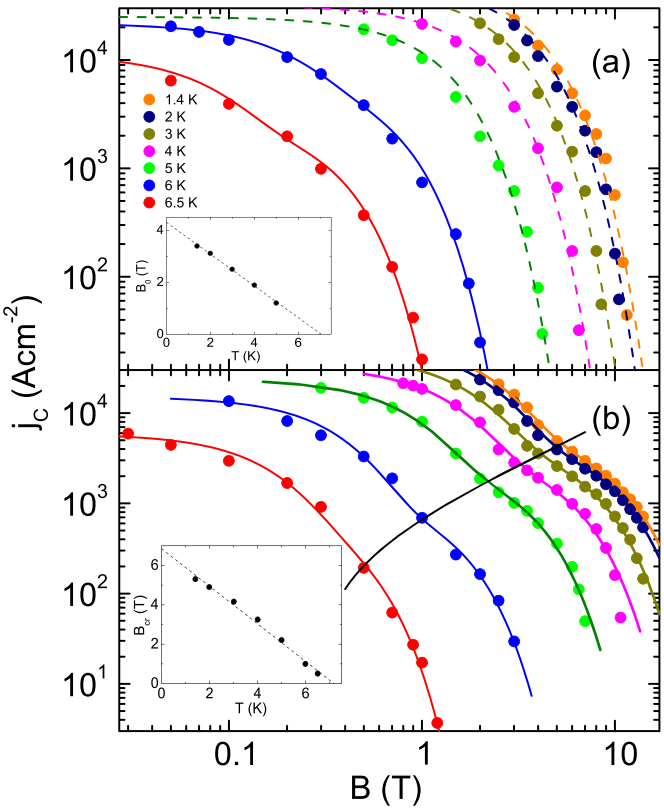

Figure 13. $j_c(B)$ (full symbols) for B parallel to the film surface (a) and B normal to the film surface (b) at temperatures from 1.4 K to 6.5 K. The dashed lines in (a) are exponential fits $j_c(B) = j_c(0) \times \exp\left[-(B/B_0)^{3/2}\right]$. The inset in (a) shows the temperature dependence of the normalization field B_0. The solid lines in (a) and (b) represent a superposition $j_c(B) = A_1 \exp\left[-(B/B_1)^{3/2}\right] + A_2 \exp\left[-(B/B_2)^{3/2}\right]$ with temperature-dependent coefficients A_1, B_1, A_2, B_2. The cross-line in (b) connects the $j_c(B_{cr}, T)$ points where the curves have an indentation. The crossover field B_{cr} versus T is displayed in the inset of (b).

Fe-based high-temperature superconductor $NaFe_{1-x}Co_xAs$ [86]. According to [81] positive curvature and enhanced linearity of $B_{c2}(T)$ is an intrinsic phenomenon in 2H-$NbSe_2$ not due to the charge density wave and not due to sample inhomogeneities. The properties can be explained by the anisotropy of the Fermi surface, that consists of open hole- and electron-like undulating cylinders with an additional closed hole-like pocket, and by a strong anisotropy of the electron-phonon interaction in layer compounds [79]. A dimensional crossover from bulk-like to 2D-like is also expected to produce a characteristic positive curvature at least in $B_{c2}^{\parallel}(T)$ [87].

The crossing point at 6.4 K and 2 T in our thin-film data remains elusive. A relation $B_{c2}^{\perp} > B_{c2}^{\parallel}$ is also reported in [36] for bulk-like polycrystalline 2H-$NbSe_2$ thin films (see dotted lines in figure 12). The authors argue that $B_{c2}^{\perp} > B_{c2}^{\parallel}$ is reasonable if 2D-flakes consisting of a few parallel Se-Nb-Se layers are to a large extent stacked vertically on the substrate and form a 3D-network with other randomly tilted flakes. Such a particular microstructure is indeed observed in our thin films, as shown in figure 4.

3.4.4. Critical current density. The critical current densities $j_c(B, T)$ are plotted in figures 13(a) and (b) for B parallel and normal to the film surface, respectively, at various temperatures between 1.4 K and 6.5 K. At each temperature the critical current densities for both field orientations decrease over two orders of magnitude from 0.1 T to 10 T. The decay of j_c with increasing field is apparently stronger for the parallel field configuration. The dashed lines in figure 13(a) for temperatures up to 5 K are exponential-decay fits $j_c(B) = j_c(0) \exp\left[-(B/B_0)^{3/2}\right]$ with the normalization field B_0. The strong exponential decay is typical for pinning of small bundles of vortices in contrast to pinning of single vortices where a power-law dependence of $j_c(B)$ is expected [88]. The exponential dependence is distinctive of collective pinning with randomly distributed pinning centers [89]. The normalization field B_0 is temperature dependent as illustrated in the inset of figure 13(a). B_0 decreases linearly from 3.4 T at 1.4 K to 1.2 T at 5 K.

The data points at 6 K and 6.5 K cannot be fitted by the simple function above. A fit succeeds only with a superposition of two exponential functions

$$j_c(B) = A_1 \exp\left[-(B/B_1)^{3/2}\right] + A_2 \exp\left[-(B/B_2)^{3/2}\right]$$

with temperature-dependent coefficients A_1, B_1, A_2, and B_2.

The fitting curves have an indentation at a crossover field B_{cr}. This feature becomes very clear in figure 13(b) for the

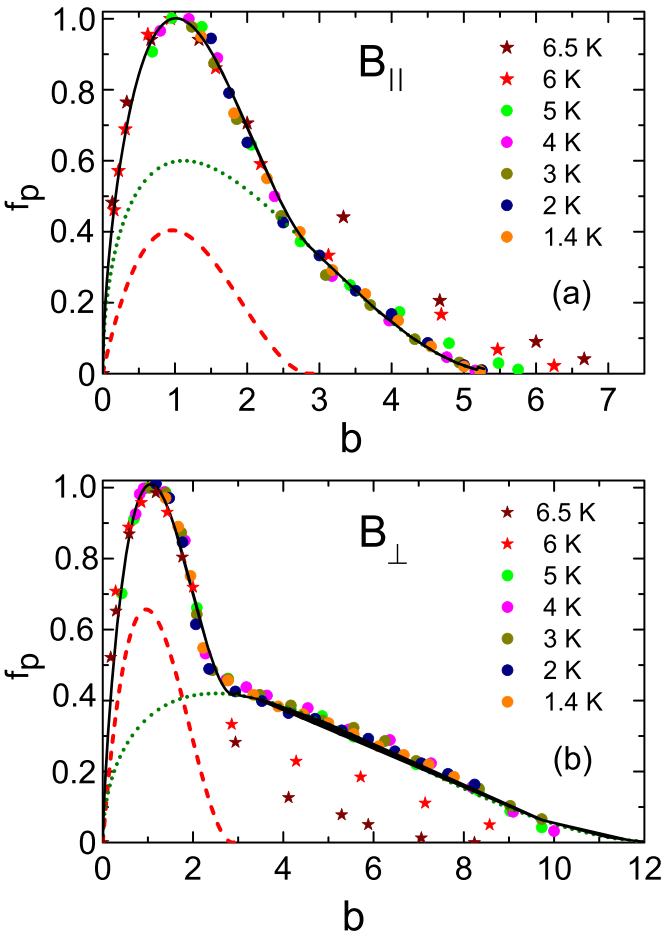

Figure 14. Reduced pinning force density $f_p = F_p/F_{p\,max}$ versus the reduced field $b = B/B_{max}$ (full symbols) with the temperature as a parameter for B parallel to the film surface (a) and B normal to the film surface (b). The dashed and dotted lines result from normal point pinning and normal surface pinning, respectively. The solid lines through the data points represent superpositions of 40% normal point pinning plus 60% normal surface pinning in (a) and 60% normal point pinning plus 40% normal surface pinning in (b).

normal field orientation at all the temperatures. The solid lines are two-exponential-function fits to the data points, and the cross-line connects the points where the indentation occurs in dependence on temperature. $B_{cr}(T)$ is displayed in the inset of figure 13(b). It decreases linearly from 5.3 T at 1.4 K to 0.5 T at 6.5 K.

Scaling the pinning force density $F_p(T, B) = j_c B$ in the mixed state of a type II superconductor is useful in the study of pinning mechanisms [90]. The figures 14(a) and (b) show the scaling of the reduced pinning force density $f_p = F_p/F_{p\,max}$ with $b = B/B_{max}$ for both field orientations. $F_{p\,max}(B_{max})$ are the maxima of the experimental $F_p(B)$ functions with T as a parameter (not shown here). Apart from the data points above $b = 3$ and 5 K all the points lie on unique master curves. The significance of these curves is that the critical current density is governed by specific types of pinning [91]. The type of pinning is revealed by the characteristic functional form of $f_p(B)$ which is sensitive to the pin strength and spacing [92]. The positions of the peaks in $f_p(B)$ in the figures at low b hint to strong, closely spaced pins. The generic functional form with B_{max} as the scaling field is $f_p(B) = Cb^p(1 - Db)^q$ [93]. The solid lines, that fit the data points in figure 14, are the result of a superposition of two pinning types: normal point pinning ($p = 1$, $q = 2$, dashed lines) and normal surface pinning ($p = 0.5$, dotted lines). The weights of normal point pinning and normal surface pinning are approximately 40% and 60%, respectively, in figure 14(a) and vice versa in figure 14(b). Above $b = 3$ and below 5 K normal surface pinning is apparently the mere mechanism for both field orientations.

The $j_c(B, T)$ measurements and their analysis are also based on our work published in [38] (cf 3.3.2). It is worth comparing the results: for the FeSe thin films in [38] no indentation of the $j_c(B, T)$ curves was observed. The data could be described by a power-law fit below a crossover field and an exponential-decay fit above. Only one type of pinning was identified, namely normal surface pinning on grain boundaries.

4. Summary and conclusions

A novel preparation method is presented where a precursor Nb thin film is rapidly selenized under high vacuum mostly avoiding contamination with nitrogen, oxygen, and moisture. In the near future a complete *in situ* process will be realized without exposing the precursor film to ambient air. In principle the process may enable the growth of epitaxial thin films by the choice of suitable substrates and adopted process parameters. It is encouraging for material systems consisting of metals and high-vapor pressure components, e.g. transition metal sulfides, selenides, and tellurides such as WS_2, $TaSe_2$, or $MoTe_2$.

The polycrystalline films grow predominantly in the hexagonal 2H-$NbSe_2$ phase. Their microstructure is extraordinary: flake-like flat grains are substantially stacked vertically on the substrate with 3D interconnection.

The main results of the electronic transport measurements can be summarized as follows:

The resistivity anomaly at 32 K and the sharp drop at 7.3 K reveal the onset of the coexisting CDW and superconducting phases, respectively.

The resistive transition to superconductivity in a magnetic field is analyzed in terms of thermally assisted flux flow with the result of a quasi 2D pancake vortex matter as expected for layered superconductors.

The linear magnetoresistance in the CDW phase is possibly triggered by the CDW order and hints at the existence of high-mobility Dirac fermions.

According to the Hall coefficient and magnetoresistance measurements the electronic transport is dominated by holes of high density and low mobility and electrons of much lower density and higher mobility. The temperature dependent Hall coefficient starts to drop at the onset of the CDW order without sign reversal.

The temperature dependence of the upper critical field is characterized by a change from positive curvature to linear behavior that seems to be an intrinsic phenomenon in 2H-$NbSe_2$. The linearity can be explained by the anisotropy of

the Fermi surface and the electron-phonon interaction. The anisotropy of the upper critical field can be related to the extraordinary microstructure of the films.

Depending on field direction, field strength, and temperature range the critical current density can be described by strong exponential decay or a superposition of two exponential functions taking the noticeable indentation into account. The critical current density is determined by a superposition of normal point and normal surface pinning with strong, closely spaced pinning centers. Normal surface pinning dominates at low temperature and high fields.

Data availability statement

All data that support the findings of this study are included within the article (and any supplementary files).

ORCID iDs

D Fuchs https://orcid.org/0000-0002-0044-7772
R Schneider https://orcid.org/0000-0003-2563-8185

References

[1] Zhou J *et al* 2018 *Nature* **556** 355
[2] Vogel E M and Robinson J A 2015 *Mater. Res. Bull.* **40** 558
[3] Revolinsky E, Brown B E, Beernsten D J and Armitage C H 1965 *J. Less-Common Met.* **8** 63
[4] Brown B E and Beernsten D J 1965 *Acta Cryst.* **18** 31
[5] Kolobov A V and Tominaga J 2016 *Two-Dimensional Transition-Metal Dichalcogenides* (*Springer Series in Materials Science* vol 239) (Springer) ch 4
[6] Revolinsky E, Spiering G A and Beernsten D J 1965 *J. Phys. Chem. Solids* **26** 1029
[7] Borisenko S V *et al* 2009 *Phys. Rev. Lett.* **102** 166402
[8] Zehetmayer M and Weber H W 2010 *Phys. Rev.* B **82** 014524
[9] Suderow H, Tissen V G, Brison J P, Martínez J L and Vieira S 2005 *Phys. Rev. Lett.* **95** 117006
[10] Kobayashi N, Noto K and Muto Y 1977 *J. Low Temp. Phys.* **27** 217
[11] Tsen A W, Hunt B, Kim Y D, Yuan Z J, Jia S, Cava R J, Hone J, Kim P, Dean C R and Pasupathy A N 2016 *Nat. Phys.* **12** 208
[12] Xi X, Wang Z, Zhao W, Park J-H, Law K T, Berger H, Forró L, Shan J and Mak K F 2016 *Nat. Phys.* **12** 139
[13] Weber F, Rosenkranz S, Heid R and Said A H 2016 *Phys. Rev. B* **94** 140504(R)
[14] Ugeda M M *et al* 2016 *Nat. Phys.* **12** 92
[15] Rahn D J, Hellmann S, Kalläne M, Sohrt C, Kim T K, Kipp L and Rossnagel K 2012 *Phys. Rev.* B **85** 224532
[16] Soumyanarayanan A, Yee M M, He Y, van Wenzel J, Rahn D J, Rossnagel K, Hudson E W, Norman M R and Hoffman J E 2013 *Proc. Natl Acad. Sci. USA* **110** 1623
[17] Wang C, Giambattista B, Slough C G, Coleman R V and Subramanian M A 1990 *Phys. Rev.* B **42** 8890
[18] Tsang J C, Smith J E and Shafer M W 1976 *Phys. Rev. Lett.* **37** 1407
[19] Kiss T, Yokoya T, Chainani A, Shin S, Hanaguri T, Nohara M and Takagi H 2007 *Nat. Phys.* **3** 720
[20] Du C H, Lin W J, Su Y, Tanner B K, Hatton P D, Casa D, Keimer B, Hill J P, Oglesby C S and Hohl H 2000 *J. Phys.: Condens. Matter* **12** 5361
[21] Zhu X, Cao Y, Zhang J, Plummer E W and Guo J 2015 *Proc. Natl Acad. Sci. USA* **112** 2367
[22] Wilson J A, Disalvo F J and Mahajan S 1974 *Phys. Rev. Lett.* **32** 882
[23] Rice T and Scott G K 1975 *Phys. Rev. Lett.* **35** 120
[24] Nicolosi V, Chhowalla M, Kanatzidis M G, Strano M S and Coleman J N 2013 *Science* **340** 1420
[25] Eda G, Yamaguchi H, Voiry D, Fujita T, Chen M and Chhowalla M 2011 *Nano Lett.* **11** 5111
[26] El-Bana M S, Wolverson D, Russo S, Balakrishnan G, Mck Paul D and Bending S J 2013 *Supercond. Sci. Technol.* **26** 125020
[27] Li Z J, Gao B F, Zhao J L, Xie X M and Jiang M H 2014 *Supercond. Sci. Technol.* **27** 015004
[28] Toshida M, Ye J, Nishizaki T, Kobayashi N and Iwasa Y 2016 *Appl. Phys. Lett.* **108** 202602
[29] Joensen P, Frindt F R and Morrison S R 1986 *Mater. Res. Bull.* **21** 457
[30] Hotta T, Tokuda T, Zhao S, Watanabe K, Taniguchi T, Shinohara H and Kitaura R 2016 *Appl. Phys. Lett.* **109** 133101
[31] Yamamoto H, Yoshii K, Saiki K and Koma A 1994 *J. Vac. Sci. Technol.* A **12** 125
[32] Wang H *et al* 2017 *Nat. Commun.* **8** 394
[33] Zou Y-C, Chen Z-G, Zhang E, Xiu F, Matsumura S, Yang L, Hong M and Zou J 2017 *Nanoscale* **9** 16591
[34] Lin H, Zhu Q, Shu D, Lin D, Xu J, Huang X, Shi W, Xi X, Wang J and Gao L 2019 *Nat. Mater.* **18** 602
[35] Shi Y, Li H and Li L-J 2015 *Chem. Soc. Rev.* **44** 2744
[36] Takahashi T, Ando C, Saito M, Miyata Y, Nakanishi Y, Pu J and Takenobu T 2021 *npj 2D Mater. Appl.* **5** 31
[37] Bosi M 2015 *RSC Adv.* **5** 75500
[38] Schneider R, Zaitsev A G, Fuchs D and Hott R 2019 *Supercond. Sci. Technol.* **32** 025001
[39] Van der Pauw L J 1958 *Philips Res. Rep.* **13** 1
[40] Roberts B W 1976 *J. Phys. Chem. Ref. Data* **5** 581
[41] Koon D W 1989 *Rev. Sci. Instrum.* **60** 271
[42] Kadijk F, Huisman R and Jellinek F 1964 *Recueil* **83** 768
[43] Naik I and Rastogi A K 2011 *Pramana J. Phys.* **76** 957
[44] Naito M and Tanaka S 1982 *J. Phys. Soc. Japan* **51** 219
[45] Long J R, Bowen S P and Lewis N E 1977 *Solid State Commun.* **22** 363
[46] Wilson A H 1938 *Proc. R. Soc.* A **167** 580
[47] Staley N E, Wu J, Eklund P, Liu Y, Linjun L and Xu Z 2009 *Phys. Rev.* B **80** 184505
[48] Iwaya K, Hanaguri T, Koizumi A, Takaki K, Maeda A and Kitazawa K 2003 *Physica* B **329–333** 1598
[49] Antonova E A, Medvedev S A and Shebalin I Y 1970 *Sov. Phys.—JETP* **30** 181
[50] De Gennes P G 1964 *Rev. Mod. Phys.* **36** 225
[51] Ogale S B, Dijkamp D, Venkatesan T, Wu X D and Inam A 1987 *Phys. Rev.* B **36** 7210
[52] Kosse A I, Kuzovlev Yu E, Levchenko G, G, Medvedev Yu V, Prokhorov Yu A, Khokhlov V A and Mikheenko P N 2003 *JETP Lett.* **78** 379
[53] Pautrat A, Scola J, Goupil C, Simon C, Villard C, Domengès B, Simon Y, Guilpin C and Méchin L 2004 *Phys. Rev.* B **69** 224504
[54] Palecchi I, Tropeano M, Lamura G, Pani M, Palombo M, Palenzona A and Putti M 2012 *Physica* C **482** 68
[55] Kes P H, Aarts J, van den Berg J, van der Beek C J and Mydosh J A 1989 *Supercond. Sci. Technol.* **1** 242
[56] Feigel'man M V, Geshkenbein V B and Larkin A I 1990 *Physica* C **167** 177
[57] Bardeen J and Stephen M J 1965 *Phys. Rev.* A **140** 1197
[58] Ichinokura S, Nakata Y, Sugawara K, Endo Y, Takayama A, Takahashi T and Hasegawa S 2019 *Phys. Rev.* B **99** 220501(R)

[59] Qiu X G, Wuyts B, Maenhoudt M, Moshchalkov V V and Bruynseraede Y 1995 *Phys. Rev.* B **52** 559
[60] Abrikosov A A 1988 *Fundamentals of the Theory of Metals* (North-Holland)
[61] Roeske J F, Shanks H R and Finnemore D K 1977 *Phys. Rev.* B **16** 3929
[62] Hambourger P D and Lewis N E 1978 *Solid State Commun.* **28** 187
[63] Reitz J R and Overhauser A W 1968 *Phys. Rev.* **171** 749
[64] Xu R, Husmann A, Rosenbaum T F, Saboungi M L, Enderby J E and Littlewood P B 1997 *Nature* **390** 57
[65] Novoselov K S, Geim A K, Mozorov S V, Jiang D, Katnelson M I, Grigorieva I V, Dubonos S V and Firsov A A 2005 *Nature* **438** 197
[66] Wang K, Graf D, Lei H, Tozer S W and Petrovic C 2011 *Phys. Rev.* B **84** 220401
[67] Taskin A A, Ren Z, Sasaki S, Segawa K and Ando Y 2011 *Phys. Rev. Lett.* **107** 016801
[68] Huynh K K, Tanabe Y and Tanigaki K 2011 *Phys. Rev. Lett.* **106** 217004
[69] Sun Y, Taen T, Yamada T, Pyon S, Nishizaki T, Shi Z and Tamegai T 2014 *Phys. Rev.* B **89** 144512
[70] Abrikosov A A 1998 *Phys. Rev.* B **58** 2788
[71] Lee H N S, McKinzie H, Tannhauser D S and Wold A 1969 *J. Appl. Phys.* **40** 602
[72] Huntley D J and Frindt R F 1974 *Can. J. Phys.* **52** 861
[73] Li L, Xu Z, Shen J, Qiu L and Gan Z 2005 *J. Phys.: Condens. Matter* **17** 493
[74] Xi X, Berger H, Forró L, Shan J and Mak K F 2016 *Phys. Rev. Lett.* **117** 106801
[75] Hurd C M 1972 *The Hall Effect in Metals and Alloys* (Plenum Press)
[76] Kim J S 1999 *J. Appl. Phys.* **86** 3187
[77] Wilson A H 1953 *The Theory of Metals* (Cambridge University Press)
[78] Leupold H A, Rothwarf F, Winter J J, Breslin J T, Ross R L and AuCoin T R 1974 *J. Appl. Phys.* **45** 5399
[79] Woolam J A, Somoano R B and O'Connor P 1974 *Phys. Rev. Lett.* **32** 712
[80] Toyota N, Nakasuji H, Noto K, Hashi A, Kobayashi N, Muto Y and Onodera Y 1976 *J. Low Temp. Phys.* **25** 485
[81] Dalrymple B J and Prober D E 1984 *J. Low Temp. Phys.* **56** 545
[82] Sanchez D, Junod A, Muller J, Berger H and Lévy F 1995 *Physica* B **204** 167
[83] Karkut M G, Matijasevic V, Antognazza L, Triscone J-M, Missert N, Beasley M R and Fischer Ø 1988 *Phys. Rev. Lett.* **60** 1751
[84] Dalichaouch Y, Lee B W, Seaman C L, Markert J T and Maple M B 1990 *Phys. Rev. Lett.* **64** 599
[85] Gantmakher V F, Klinkova L A, Barkovskii N V, Tsydynzhapov G E, Wiegers S and Geim A K 1996 *Phys. Rev.* B **54** 6133
[86] Ghannadzadeh S, Wright J D, Foronda F R, Blundell S J, Clarke S J and Goddard P A 2014 *Phys. Rev.* B **89** 054502
[87] Klemm R A, Luther A and Beasley M R 1975 *Phys. Rev.* B **12** 877
[88] Qin M J, Wang X L, Liu H K and Dou S X 2002 *Phys. Rev.* B **65** 132508
[89] Larkin A I and Ovchinnikov Y N 1979 *J. Low Temp. Phys.* **34** 409
[90] Fietz W A and Webb W W 1969 *Phys. Rev.* **178** 657
[91] Ullmaier H 1975 *Irreversible Properties of Type II Superconductors* (Springer)
[92] Dew-Hughes D 1974 *Phil. Mag.* **30** 293
[93] Shigeta I, Abiru T, Abe K, Nishida A and Matsumoto Y 2003 *Physica* C **392–396** 359